The Astrophysical Journal, 978:99 (13pp), 2025 January 01 https://doi.org/10.3847/1538-4357/ad96b3

Thorium in Kilonova Spectra: Exploring the Heaviest Detectable Element

Nanae Domoto[1], Shinya Wanajo[1,2,3], Masaomi Tanaka[1,4], Daiji Kato[5,6], and Kenta Hotokezaka[7,8]

[1] Astronomical Institute, Tohoku University, Aoba, Sendai 980-8578, Japan; n.domoto@astr.tohoku.ac.jp
[2] Max-Planck-Institut für Gravitationsphysik (Albert-Einstein-Institut), Am Mühlenberg 1, D-14476 Potsdam-Golm, Germany
[3] Interdisciplinary Theoretical and Mathematical Sciences Program (iTHEMS), RIKEN, Wako, Saitama 351-0198, Japan
[4] Division for the Establishment of Frontier Sciences, Organization for Advanced Studies, Tohoku University, Sendai 980-8577, Japan
[5] National Institute for Fusion Science, 322-6 Oroshi-cho, Toki 509-5292, Japan
[6] Interdisciplinary Graduate School of Engineering Sciences, Kyushu University, Kasuga, Fukuoka 816-8580, Japan
[7] Research Center for the Early Universe, Graduate School of Science, University of Tokyo, Bunkyo, Tokyo 113-0033, Japan
[8] Kavli IPMU (WPI), UTIAS, The University of Tokyo, Kashiwa, Chiba 277-8583, Japan

Received 2024 August 06; revised 2024 October 26; accepted 2024 November 24; published 2024 December 27

Abstract

Kilonova spectra provide us with direct information about rapid neutron-capture nucleosynthesis (*r*-process) in neutron star (NS) mergers. In this paper, we study the signatures of elements beyond the third *r*-process peak expected to be produced in neutron-rich ejecta in the photospheric spectra of kilonova. We select Ra II, Ac III, and Th III as our candidates because they have a small number of valence electrons and low-lying energy levels, which tend to result in strong absorption features. We systematically calculate the strength of bound–bound transitions of these candidates by constructing a line list based on the available atomic database. We find that Th III is the most promising species, showing strong transitions at near-infrared wavelengths. By performing radiative transfer simulations, we find that Th III produces broad absorption features at ∼18000 Å in the spectra when the mass ratio of actinides to lanthanides is larger than the solar *r*-process ratio and the mass fraction of lanthanides is $\lesssim 6 \times 10^{-4}$. Our models demonstrate that the Th feature may be detectable if the bulk of the ejecta in the line-forming region is dominated by relatively light *r*-process elements with the mixture of a small fraction of very neutron-rich material. Such conditions may be realized in the mergers of unequal-mass NSs or black hole–NS binaries. To detect the Th absorption features, observations from space (such as with the JWST) or high-altitude sites are important as the wavelength region of the Th features overlaps with that affected by strong telluric absorption.

Unified Astronomy Thesaurus concepts: R-process (1324); Radiative transfer simulations (1967); Atomic physics (2063); Transient sources (1851)

1. Introduction

Coalescence of binary neutron stars (NSs) is a promising site of rapid neutron-capture nucleosynthesis (*r*-process; e.g., J. M. Lattimer & D. N. Schramm 1974; D. Eichler et al. 1989; C. Freiburghaus et al. 1999; S. Goriely et al. 2011; O. Korobkin et al. 2012; S. Wanajo et al. 2014). Radioactive decay of freshly synthesized nuclei in the ejected neutron-rich material powers electromagnetic emission, called a kilonova (L.-X. Li & B. Paczyński 1998; B. D. Metzger et al. 2010; L. F. Roberts et al. 2011). In 2017, associated with the detection of gravitational waves (GWs) from an NS merger (GW170817; B. P. Abbott et al. 2017a), an electromagnetic counterpart was identified (AT2017gfo; B. P. Abbott et al. 2017b). The observed properties of AT2017gfo at ultraviolet (UV), optical, and near-infrared (NIR) wavelengths are consistent with the theoretical expectation of a kilonova (e.g., I. Arcavi et al. 2017; D. A. Coulter et al. 2017; P. A. Evans et al. 2017; E. Pian et al. 2017; S. J. Smartt et al. 2017; Y. Utsumi et al. 2017; S. Valenti et al. 2017). This electromagnetic counterpart has provided us with evidence that NS mergers are sites of *r*-process nucleosynthesis (e.g., D. Kasen et al. 2017; A. Perego et al. 2017; M. Shibata et al. 2017; M. Tanaka et al. 2017; K. Kawaguchi et al. 2018; S. Rosswog et al. 2018).

Recent advances in the study of kilonova spectra have enabled the direct identification of individual elements. In the photospheric spectra at an early phase, one can identify the synthesized elements from the absorption features. D. Watson et al. (2019) first reported that the absorption features around $\lambda \sim 8000$ Å in the photospheric spectra of AT2017gfo could be explained by Sr II ($Z = 38$). This has been further supported by independent analyses (N. Domoto et al. 2021; J. H. Gillanders et al. 2022), although the same features may be caused by He I (A. Perego et al. 2022; Y. Tarumi et al. 2023; but see also A. Sneppen et al. 2024). N. Domoto et al. (2022) reported the absorption features at $\lambda \sim 13000$ and 14500 Å in the spectra of AT2017gfo as to be caused by La III ($Z = 57$) and Ce III ($Z = 58$), respectively. The identification of Ce III has been further supported by another approach using stellar spectra that show strong Ce III absorption (N. Domoto et al. 2023; M. Tanaka et al. 2023). Furthermore, A. Sneppen & D. Watson (2023) interpreted the marginal absorption features at $\lambda \sim 7600$ Å as to be caused by Y II ($Z = 39$), although Q. Pognan et al. (2023) suggested the same features were due to Rb I ($Z = 37$).

In the nebula spectra at a late phase, one can also identify the elements from emission features. K. Hotokezaka et al. (2023) studied the spectra of AT2017gfo >7 days after the merger, and reported the emission features at $\lambda \sim 2.1\ \mu$m as to be caused by Te III ($Z = 52$). In GW170817, the detection of nebular emission at 4.5 μm and the upper limit at 3.6 μm by the Spitzer space telescope at very late phases were reported (V. A. Villar et al. 2018; M. M. Kasliwal et al. 2022), which suggests the distinctive spectral shape. It has been suggested that these features may be explained by Se ($Z = 34$) or W ($Z = 74$; K. Hotokezaka et al. 2022), although conclusive spectroscopic identification has not been made.

Despite the identification of these elements in the spectra of AT2017gfo, the overall abundance pattern in this NS merger event is not yet clear. It is expected that so-called third *r*-process peak elements, e.g., Pt and Au ($Z = 78$, 79), have been abundantly synthesized by this event (e.g., S. Goriely et al. 2011; O. Korobkin et al. 2012; S. Wanajo et al. 2014). In fact, J. H. Gillanders et al. (2021) searched for the signatures of Pt and Au in the spectra of AT2017gfo, but concluded that these elements do not produce prominent line features. There is currently no established way to identify these elements with spectroscopic observations.

The very neutron-rich ejecta of a NS merger is expected to produce actinides (e.g., I. Kullmann et al. 2023; S. Fujibayashi et al. 2023). It has been proposed that one can trace such heavy nuclei by the late-time bolometric light curve, as the radioactive heating is often dominated by a few isotopes with half-lives of 10–100 days (Y. Zhu et al. 2018; M.-R. Wu et al. 2019). However, such a constraint was difficult for AT2017gfo due to the limited observations in the late phase. Also, N. Domoto et al. (2022) briefly discussed the spectral feature caused by an actinide, Th ($Z = 90$). They found that Th produces the absorption feature at $\lambda \sim 18000$ Å, although the feature is not as prominent as those of lanthanides. However, they used only one abundance model dominated by relatively light *r*-process elements and did not investigate the conditions that give rise to the Th features in detail. Furthermore, they did not investigate the features of heavy elements around actinides other than Th, such as Ra and Ac. Since the detection of such elements provides us with unambiguous evidence that heavy *r*-process nuclei are synthesized in NS mergers, it is important to clarify the detectability of these features.

In this paper, we explore the detectability of absorption features caused by the elements beyond the third *r*-process peak in photospheric spectra of kilonovae. In particular, motivated by the finding in N. Domoto et al. (2022), we study the absorption features caused by Th III at $\lambda \sim 18000$ Å in the spectra in detail. In Section 2, we first systematically calculate the strength of bound–bound transitions of candidate species to show that Th III is the most plausible element among candidates as the source of absorption features. Then, in Section 3, we perform radiative transfer simulations of NS merger ejecta and investigate the conditions in which we can find the absorption features of Th III. The implications and caveats of our results are discussed in Section 4. Finally, we give our conclusions in Section 5.

2. Th III and Other Candidate Species

We first consider the heaviest candidate species that may produce absorption features in kilonova photospheric spectra. It has been shown that the elements on the left side of the periodic table, such as Ca, Sr, La, and Ce, tend to produce absorption features in the spectra (N. Domoto et al. 2022). This is explained by their atomic properties: a small number of valence electrons for which transition probabilities (or weighted oscillator strength, *gf*-values) tend to be larger, and low-lying energy levels for which the electron population tends to be higher (see Section 2.2). Among the elements beyond the third *r*-process peak, Ra II ($Z = 88$), Ac III ($Z = 89$), and Th III ($Z = 90$) are plausible candidates to produce absorption features, because their atomic structures are expected to be analogous to those of Ca II/Sr II, La III, and Ce III, respectively. Note that Ra and Ac are radioactive elements, but their isotopes with relatively long half-lives (on order of days or longer) can exist in NS merger ejecta at a few days after the merger. In the following subsections, however, we will show that Th III is the only plausible candidate for the absorption features.

2.1. Line List

To evaluate the strength of bound–bound transitions, relevant atomic data, i.e., a set of transition wavelengths, energy levels of transitions, and *gf*-values are necessary. In this paper, we use the "hybrid" line list from N. Domoto et al. (2022, 2023) as a baseline. This line list consists of the theoretically calculated data for the elements $Z = 30$–88 (M. Tanaka et al. 2020) as well as experimentally calibrated data for the elements $Z = 20$–29 (N. E. Piskunov et al. 1995; F. Kupka et al. 1999; T. Ryabchikova et al. 2015) and for several important ions for the absorption features in kilonovae, Sr II, Y I, Y II, Zr I, Zr II, Ba II, La III, and Ce III.

Although the hybrid line list contains data for Ra II from theoretical calculations, the data were not experimentally calibrated as it was outside the scope of the study in N. Domoto et al. (2022, 2023). Fortunately, some experimental data of the transitions for Ra II are available in the NIST Atomic Spectral Database (ASD; A. Kramida et al. 2022). Some of them have *gf*-values from theoretical calculations (B. K. Sahoo et al. 2009) with high accuracy. Thus, we replace the Ra II data in the hybrid line list with the data in the NIST ASD for which the *gf*-values are available. Experimental transition data for Ac III are also available in the NIST ASD, with the *gf*-values from theoretical calculations (U. I. Safronova et al. 2007; B. M. Roberts et al. 2013) with high accuracy (A. Kramida 2022). Thus, we also add the available data for Ac III from the NIST ASD to our line list.

For Th III, experimental data for the transition wavelengths and energy levels are available for the optical to NIR region (R. J. Engleman 2003). However, while the *gf*-values of optical lines are obtained by using semi-empirical calculations (E. Biémont et al. 2002), those of NIR lines are not available. N. Domoto et al. (2022) estimated the *gf*-values of the NIR lines using the measured relative intensities I by

$$\begin{aligned} I &= b\ g_u A\ e^{-\frac{E_u}{kT}} \\ &= b \frac{8\pi e^2}{m_e c \lambda^2} g_l f_{\rm osc}\, e^{-\frac{E_u}{kT}}, \end{aligned} \tag{1}$$

where A, λ, and $f_{\rm osc}$ are Einstein's A coefficient, the transition wavelength, and the oscillator strength, g and E are the statistical weight and the energy level of the lower (l) and upper (u) levels for a transition, respectively, and b is a constant depending on the ion species. This equation is valid since the electron population in the experiments follows the Boltzmann distribution with atomic excitation temperature (B. A. Palmer & R. Engleman 1983). As the relative intensities of the measured lines are listed in the NIST ASD in a consistent way through the whole wavelength range, one can compare the calculated and measured intensities for the lines over a wide range of wavelengths.

We update the *gf*-values of the NIR lines for Th III by following N. Domoto et al. (2022), but in a more quantitative way. To calculate the intensities of the optical lines for Th III

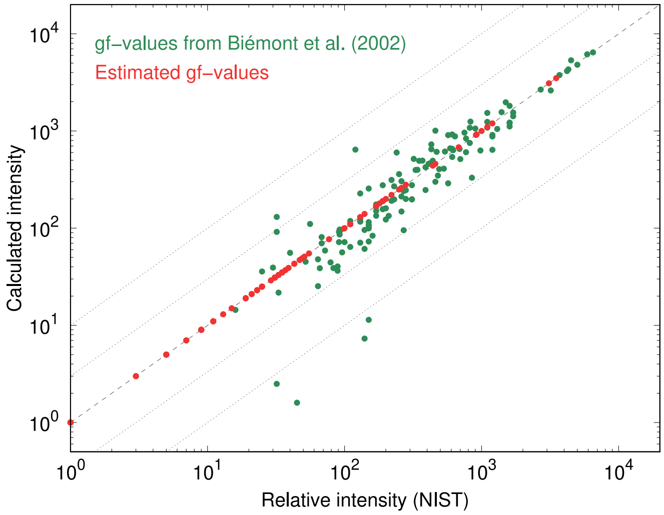

Figure 1. Comparison of intensities (green circles) for Th III lines between those calculated with *gf*-values from E. Biémont et al. (2002) and those measured by experiments (R.J. Engleman 2003; A. Kramida et al. 2022). Gray dashed and dotted lines correspond to perfect agreement and deviations by a factor of 3 and 10, respectively. Red circles indicate the lines whose *gf*-values are estimated from the measured intensities.

with known *gf*-values (E. Biémont et al. 2002) using Equation (1), N. Domoto et al. (2022) adopted the temperature $T = 5000$ K by visual inspection at which the measured and calculated intensities of the optical lines agree with each other. Instead, here we use the least-squares method to find the temperature at which the relationship of the measured and calculated intensities is closest to linear. As a result, the temperature is estimated as $T = 6000$ K, which we adopt in this study. A comparison between the measured intensities and calculated intensities using the known *gf*-values is shown in Figure 1. We then estimate the *gf*-values of the NIR lines for Th III by using this temperature of $T = 6000$ K. Consequently, the estimations of the *gf*-values are systematically smaller than those in N. Domoto et al. (2022) by up to a factor of ∼3. We summarize the estimated *gf*-values in Table 2.[9]

Note that there is a scatter between measured and calculated intensities by roughly a factor of 3, especially for the weaker lines. This can be due to uncertainty in the *gf*-values used, which is expected to be 5%–10% or more (E. Biémont et al. 2002). However, it is difficult to assess the uncertainty with lack of experimental evaluations. Also, the presence of scatter might also indicate that the electron population in the experiments does not completely follow the Boltzmann distribution. These may cause uncertainty in the temperature estimates and resulting *gf*-values of the NIR lines (see also Section 4).

We mention that some theoretical atomic data of actinides are available (R. F. Silva et al. 2022; A. Flörs et al. 2023; C. J. Fontes et al. 2023). Such data are constructed performing atomic calculations to estimate the opacity and its effect on kilonovae. Such theoretical data, however, are not calibrated with experiments, and thus they cannot be readily used to discuss spectral features. Nevertheless, those studies have shown that actinides tend to have many low-lying energy levels in comparison to lanthanides, which is consistent with the experimental results for Th III (see the next section).

2.2. *Strength of Lines for Radium, Actinium, and Thorium*

To investigate the important species for absorption features in kilonova spectra among the heaviest elements, we systematically calculate the strength of bound–bound transitions for a given set of density, temperature, and element abundances. The strength of a line is approximated by the Sobolev optical depth (V. V. Sobolev 1960) for each bound–bound transition,

$$\tau_{\rm Sob} = \frac{\pi e^2}{m_e c} n_{i,j,k} t \lambda f_{\rm osc}, \tag{2}$$

in homologously expanding ejecta. The Sobolev approximation is valid for matter with a high expansion velocity and a large radial velocity gradient. Here, $n_{i,j,k}$ is the number density of the ion at the lower level of a transition (*i*th element, *j*th ionization stage, and *k*th excited state). As in previous work on kilonovae (e.g., D. Kasen et al. 2013; M. Tanaka & K. Hotokezaka 2013), we assume LTE; we solve the Saha equation to obtain ionization states, and assume the Boltzmann distribution for the population of excited levels (see K. Hotokezaka et al. 2021; Q. Pognan et al. 2022a, for non-LTE effects).

For the abundances in ejected matter from an NS merger, we use the same model as in N. Domoto et al. (2022), which is based on the multicomponent free-expansion (mFE) model of S. Wanajo (2018). The model is constructed as an ensemble of parametrized outflows for each constant velocity, initial entropy, and initial electron fraction ($Y_{\rm e}$). Here, we use the "Light" (L) model adopted in N. Domoto et al. (2022) as our fiducial model, which approximately fits the *r*-process residuals (N. Prantzos et al. 2020) for $A = 66$–69 and 3% of those for $A = 100$–205, where A is the atomic mass number (the blue curves in Figure 2). This is motivated by the fact that the L model can reasonably explain the observed features of heavy elements such as La III and Ce III in AT2017gfo (N. Domoto et al. 2022). We refer the readers to Section 3 for discussion using a different abundance distribution. It should be noted that we do not intend this abundance pattern to represent the whole ejecta, but rather those in the line-forming regions. We use the abundances at $t = 1.5$ days for $Z = 20$–100 in our calculations. The mass fractions of elements relevant to this study are summarized in Table 1.

The Sobolev optical depths of bound–bound transitions for the L model at $t = 1.5$ days are shown in Figure 3. We evaluate the Sobolev optical depth for a density of $\rho = 10^{-14}\,{\rm g\,cm^{-3}}$ and temperatures of $T = 7000$ and 5000 K (top two panels). These are typical values in the line-forming region for the L model at 1–2 days after the merger (see Section 3). As already shown in N. Domoto et al. (2022), Ca II, Sr II, Y II, Zr II, La III, and Ce III show strong transitions.

We find that the strength of the Th III lines (light blue) at the NIR wavelengths is comparable to that of the Ce III lines (orange). This is consistent with the finding in N. Domoto et al. (2022), although the updated *gf*-values are adopted here. As briefly discussed in N. Domoto et al. (2022), many Th III lines show similar Sobolev optical depths, and none of them are outstanding. This is due to the fact that Th III has denser low-lying energy levels involved in the 5*f* shell compared to those of Ce III involved in the 4*f* shell (Figure 4). The Boltzmann factors at each level do not vary significantly among such low-

---

[9] As all the g_l-values ($= 2J_l + 1$, where J_l is the total angular momentum of the lower level) are known for the NIR lines of Th III (Table 2; see the NIST ASD for complete information), the procedure in fact gives the *f*-values, not *gf*-values, for all the NIR lines.

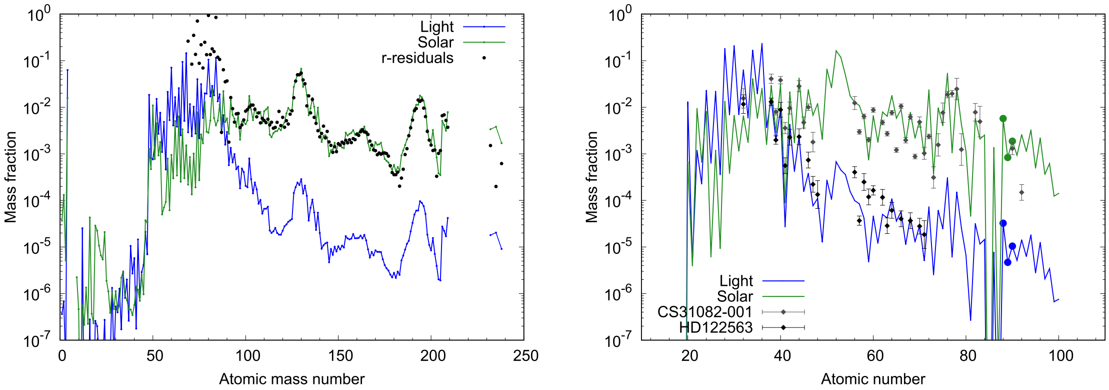

Figure 2. Left: final abundances (at 1 yr; all trans-Pb nuclei except for Th and U are assumed to have decayed) of the "Light" (L, blue) and "Solar" (S, green) models as a function of mass number. Black circles show the *r*-process residual pattern (N. Prantzos et al. 2020), which are scaled to match those for the S model at $A = 138$. Right: abundances at $t = 1.5$ days for each model as a function of atomic number. Abundances of an *r*-process-deficient star HD 122563 (black diamonds, S. Honda et al. 2006; Ge from J. J. Cowan et al. 2005; Cd and Lu from I. U. Roederer et al. 2012) and an *r*-process-enhanced star CS 31082-001 (gray diamonds; C. Siqueira Mello et al. 2013) are also shown for comparison purposes. The abundances of HD 122563 and CS 31082-001 are scaled to those for the L and S models at $Z = 40$, respectively. The elements relevant to this study are indicated by large circles in each model (see also Table 1).

Table 1
Mass Fractions of Selected Elements

Model		X (Ra)	X (Ac)	X (Th)	X (Ce)	X (lan)[a]
Light (L)	Final	⋯	⋯	1.8×10^{-5}	3.1×10^{-5}	4.6×10^{-4}
	1.5 days	3.2×10^{-5}	4.7×10^{-6}	1.0×10^{-5}	4.2×10^{-5}	5.8×10^{-4}
Solar (S)	Final	⋯	⋯	3.4×10^{-3}	5.9×10^{-3}	8.5×10^{-2}
	1.5 days	5.7×10^{-3}	8.3×10^{-4}	1.9×10^{-3}	5.7×10^{-3}	9.0×10^{-2}

Notes. The top and bottom rows in each model show the final abundances and those at $t = 1.5$ days, respectively.
[a] Sum of mass fractions for lanthanides ($Z = 57$–71).

lying levels, which makes the Sobolev optical depths of these lines similar. The variations in the Sobolev optical depths mainly reflect the variations in *gf*-values, but for the NIR range in particular the low-lying energy levels (as well as relatively high *gf*-values) enable the Th III NIR lines involving such levels (higher-level population) to show relatively large Sobolev optical depths. This is especially the case for the lines around $\lambda \sim 20000$ Å, which will be further investigated in Section 3.

For Ra II, the triplet lines are similar to those of Ca II, Sr II, and Ba II, since their atomic structures, having one electron in the *s* orbit, are analogous to each other (Figure 5). Nevertheless, the Ra II triplet lines do not show large Sobolev optical depths due to the much smaller mass fraction of Ra than those of Ca or Sr by a factor of 10^3 (Figure 2). From a nucleosynthesis point of view, it is not conceivable that Ra is more abundant than lanthanides or actinides by orders of magnitude. In the case of the solar ratio (see Table 1 and Figure 2), the mass fraction of Ra relative to individual lanthanides or Th is similar within a factor of a few at $t = 1.5$ days. Lanthanides have many lower energy levels below ∼2 eV, leading to larger Sobolev optical depths than those from Ra with similar mass fractions. Thus, even if the mass fraction of Ra is somewhat larger than that in the L model assumed here, it would not be expected that the strength of the Ra II triplet lines can compete with those of other lines for lanthanides or Th III. To fully verify this, however, we need experimentally calibrated data for more lanthanides at $\lambda \lesssim 10000$ Å.

For Ac III, the available data reside in the forest of lines at the UV and optical wavelengths (yellow lines in Figure 3). The strength of the Ac III lines are at their most comparable to those of the other optical lines of heavy elements for higher temperature. One might expect that the atomic structure of Ac III is analogous to that of La III, which shows strong transitions at NIR wavelengths. However, this is not the case according to experimentally constructed atomic data (W. F. Meggers et al. 1957; A. Kramida et al. 2022): While the ground-state electron configuration of La III is 5*d*, that of Ac III is 7*s* (Figure 6). In the case of La III, the transitions from the ground configuration (5*d*) to the first excited configuration (4*f*) are very strong at the NIR wavelengths. On the other hand, the energy differences between the 6*d* and 5*f* orbits for Ac III are large, which lead to the transition wavelengths being at the optical region. Thus, Ac III does not have (allowed) lines at the NIR wavelengths involved in low-lying energy levels.

In summary, among the elements beyond the third *r*-process peak ($Z = 88$–90), Th III is the most promising species that exhibits strong transitions in NIR wavelengths under the relevant physical conditions of NS merger ejecta. This is because Th III has many NIR lines involved in the dense low-lying energy levels. In general, the number of lines is relatively small in the NIR region compared to that in the optical region. Thus, individual NIR lines tend to be separated, resulting in recognizable features in the spectra. Hereafter, we focus on Th III and explore the absorption features caused by Th III in the NIR region.

2.3. *Temperature Dependence of Th III Lines*

We also evaluate the Sobolev optical depths of bound–bound transitions for a temperature of $T = 4000$ K. This is a typical

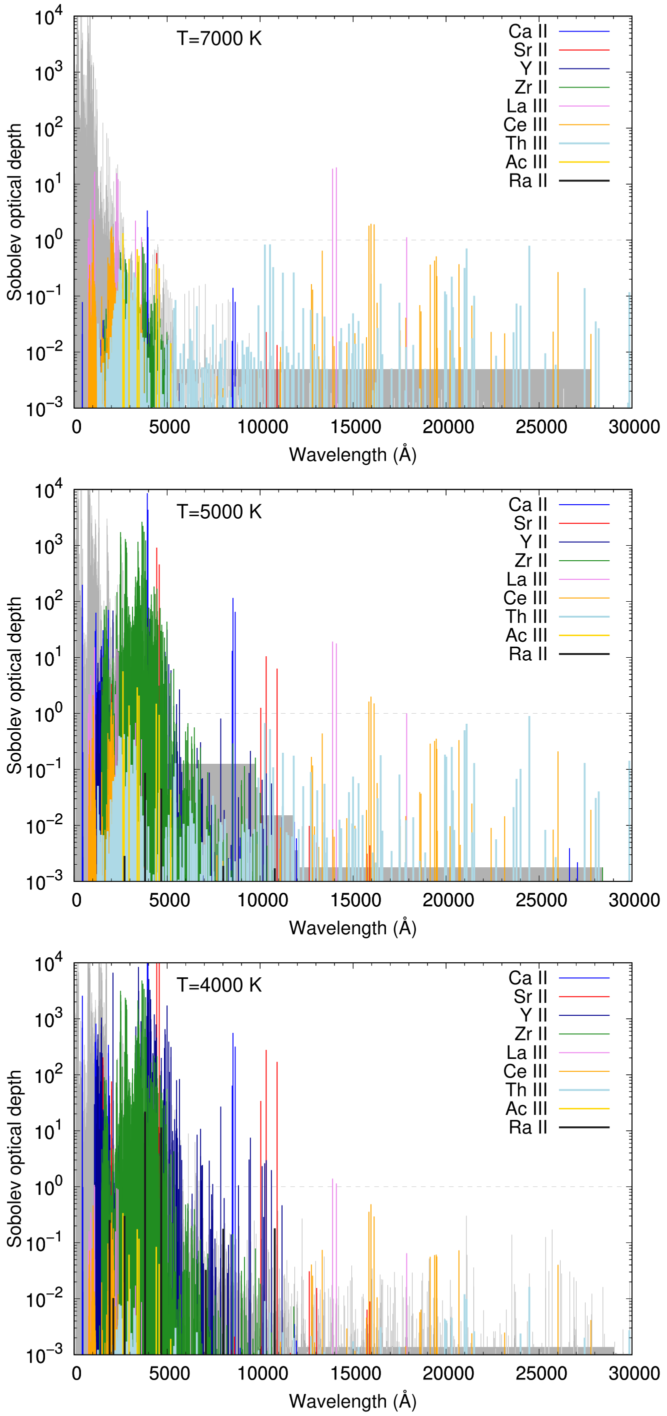

Figure 3. Sobolev optical depth of bound–bound transitions for the L model. The ions of interest with large contributions are shown with colors. The panels, from top to bottom, show results with temperatures of $T = 7000$, 5000, and 4000 K, respectively, and with a density of $\rho = 10^{-14}$ g cm^{-3} at $t = 1.5$ days.

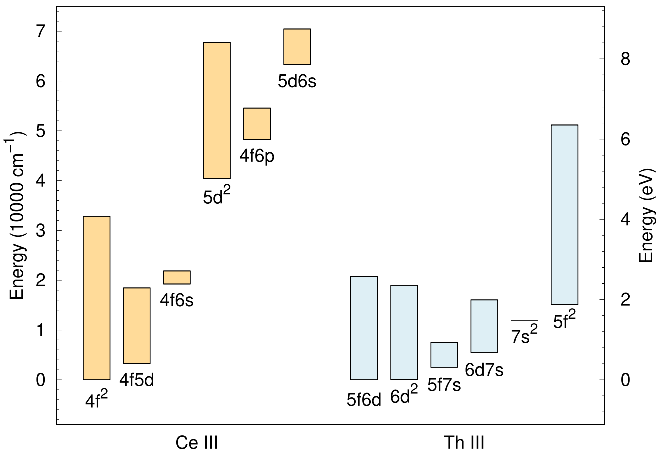

Figure 4. Energy distributions of the six low-lying configurations for Ce III (left) and Th III (right). The bottom and top edges in each box correspond to the lowest and highest energies in each configuration, respectively. The first two configurations for Ce III are involved in the NIR region, while all six configurations for Th III are involved in the NIR region.

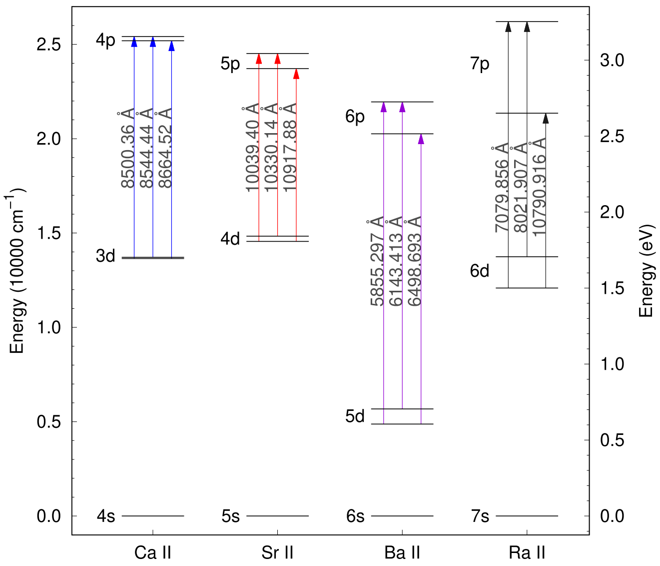

Figure 5. Energy diagrams for Ca II, Sr II, Ba II, and Ra II. Each arrow shows the triplet transition with the value of the transition wavelength (in vacuum). The energy terms for these triplet lines are $^2D_{3/2}$–$^2P^o_{3/2}$, $^2D_{5/2}$–$^2P^o_{3/2}$, and $^2D_{3/2}$–$^2P^o_{1/2}$ from shorter to longer wavelengths.

value in the line-forming region for the L model at ~3 days after merger (see Section 3). The results are shown in the bottom panel of Figure 3. We find that the Th III lines become relatively weak and almost hidden by the other lines at $T = 4000$ K. This is in contrast to the fact that the Ce III lines remain strong compared to the other lines, although their Sobolev optical depths also become smaller.

The reason why the Th III lines rapidly become weaker than the Ce III lines at lower temperature can be understood from their temperature dependences for ionization. The ionization potentials for Ce are 10.96 eV (II–III) and 20.2 eV (III–IV); those for Th are 12.10 eV (II–III) and 18.32 eV (III–IV). Figure 7 shows the ionization fractions of Ce and Th for a density of $\rho = 10^{-14}$ g cm^{-3} as a function of temperature under LTE. We find that the temperature range in which Th III exists is narrower than that for Ce III. For $T = 4000$ K, most Th ions become singly ionized (II), while ~30% of Ce III remains. Thus, the decreased fraction of the doubly ionized state results in the weak Th III lines at $T = 4000$ K.

This implies that, even if the Th III features appear with the appropriate photospheric temperature at a certain epoch, they would rapidly disappear as the ejecta temperature decreases with time. We discuss the temperature dependence for the Th III lines on the spectra in Section 3.2 in more depth.

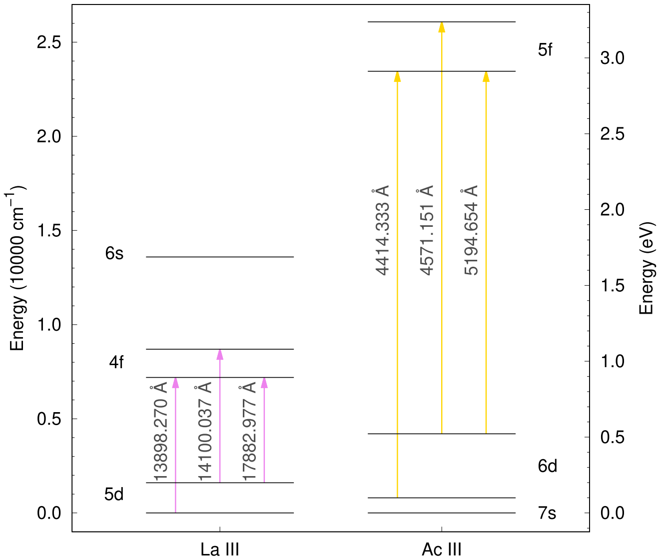

Figure 6. Energy diagrams for La III and Ac III. Each arrow shows the transition with the value of the transition wavelength (in vacuum). The energy terms for these transitions are $^2D_{3/2}$–$^2F^o_{5/2}$, $^2D_{5/2}$–$^2F^o_{7/2}$, and $^2D_{5/2}$–$^2F^o_{5/2}$ from shorter to longer wavelengths.

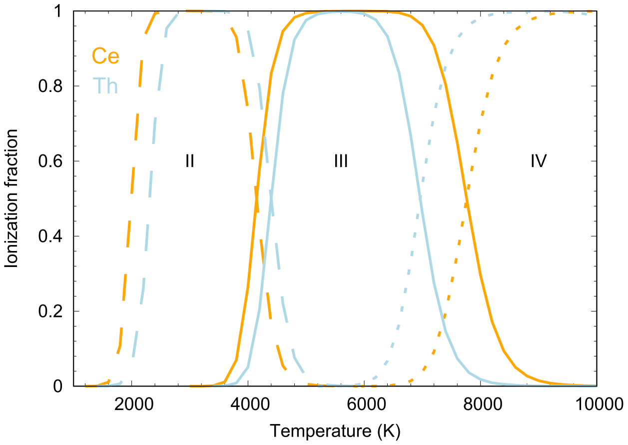

Figure 7. Ionization fractions of Ce (orange) and Th (light blue) under LTE, assuming the density of 10^{-14} g cm^{-3}. The dashed, solid, and dotted lines show the fractions of II, III, and IV, respectively.

3. Synthetic Spectra

3.1. Fiducial Cases

In this section, we calculate synthetic spectra of kilonovae to investigate the absorption features caused by Th III. We use a wavelength-dependent radiative transfer simulation code (M. Tanaka & K. Hotokezaka 2013; M. Tanaka et al. 2014, 2017; K. Kawaguchi et al. 2018, 2020). Photon transfer is calculated by the Monte Carlo method. For the atomic data with which to compute the opacity for bound–bound transitions, we use the updated line list in Section 2.1. For the detailed treatment to compute the bound–bound opacity, we refer the reader to N. Domoto et al. (2022). We assume an ejecta structure with a single power law ($\rho \propto r^{-3}$) for a velocity range of the ejecta $v = 0.05$–$0.3\,c$ (e.g., B. D. Metzger et al. 2010). The total ejecta mass is set to be $M_{\rm ej} = 0.03 M_\odot$, which is suggested to explain the observed luminosity of AT2017gfo (e.g., M. Tanaka et al. 2017; K. Kawaguchi et al. 2018).

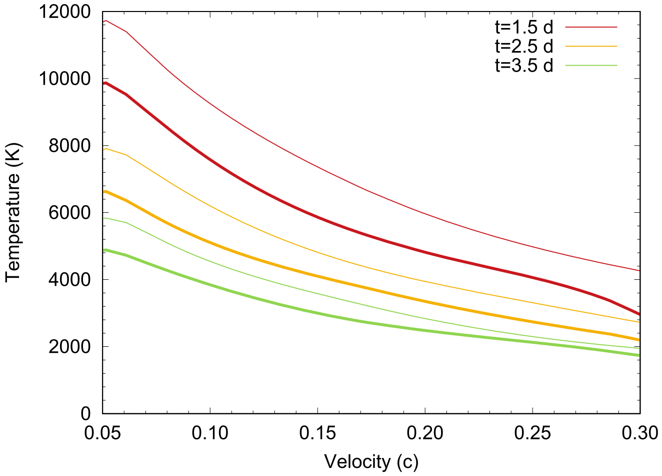

Figure 8. Temperature structures of the ejecta at $t = 1.5$, 2.5, and 3.5 days after the merger for the L (thick lines) and S (thin lines) models.

Here, we use the L model described in Section 2.2 as the fiducial model for the abundance distribution of the ejecta. For comparison purposes, we also use the "Solar" (S) model adopted in N. Domoto et al. (2021), which fits the r-process residuals for $A \geqslant 88$ (green curves in Figure 2). Note that we set the velocity range of ejecta $v = 0.05$–$0.4c$ for the S model, to avoid the photosphere at the phase of interest being located at the edge of the ejecta due to the high opacity. This results in subtle differences in density structures between models, but does not affect the discussion.

The heating rate of radioactive nuclei as a function of time is taken consistently from each abundance model. The thermalization efficiencies of γ-rays and radioactive particles follow the analytic formula given by J. Barnes et al. (2016). In the radiative transfer code, the temperature in each cell is determined by the photon flux assuming that the wavelength-integrated photon intensity $\langle J \rangle = \int J_\nu d\nu$ follows the Stefan–Boltzmann law, i.e., $\sigma T_R^4 = \pi \langle J \rangle$ (L. B. Lucy 2003; M. Tanaka & K. Hotokezaka 2013). The kinetic temperature of electrons T_e is assumed to be the same as the radiation temperature T_R, i.e., $T = T_e = T_R$ under LTE. The resulting temperature structures of the ejecta for the L and S models are shown in Figure 8.

Figure 9 shows the synthetic spectra at $t = 1.5$ days after merger for the L (left) and S (right) models. The dark blue and black curves are the original and smoothed results, respectively. To find the contributions of relevant elements to the spectra, we also plot the Sobolev optical depths in the photospheric region at $v \sim 0.13c$ for the L model and at $v \sim 0.37c$ for the S model, respectively. The wavelengths of the lines are blueshifted according to the photospheric velocities. Note that we plot only spectroscopically accurate lines for the L model, while we plot all lines, whose wavelengths are not necessarily accurate, for the S model. To clarify the effects of the Th III lines, we compare the results with the cases excluding Th III lines (dark yellow curve).

For the L model (left panel), we find that a broad absorption feature appears around $\lambda \sim 18000$ Å (light blue arrow). The clear absorption features caused by Ca II, Sr II, La III, and Ce III (blue, red, pink, and orange arrows, respectively) are also seen in the spectrum, which are unaffected by the Th III lines. This is consistent with the results in N. Domoto et al. (2022), although the updated line list of Th III is adopted here.

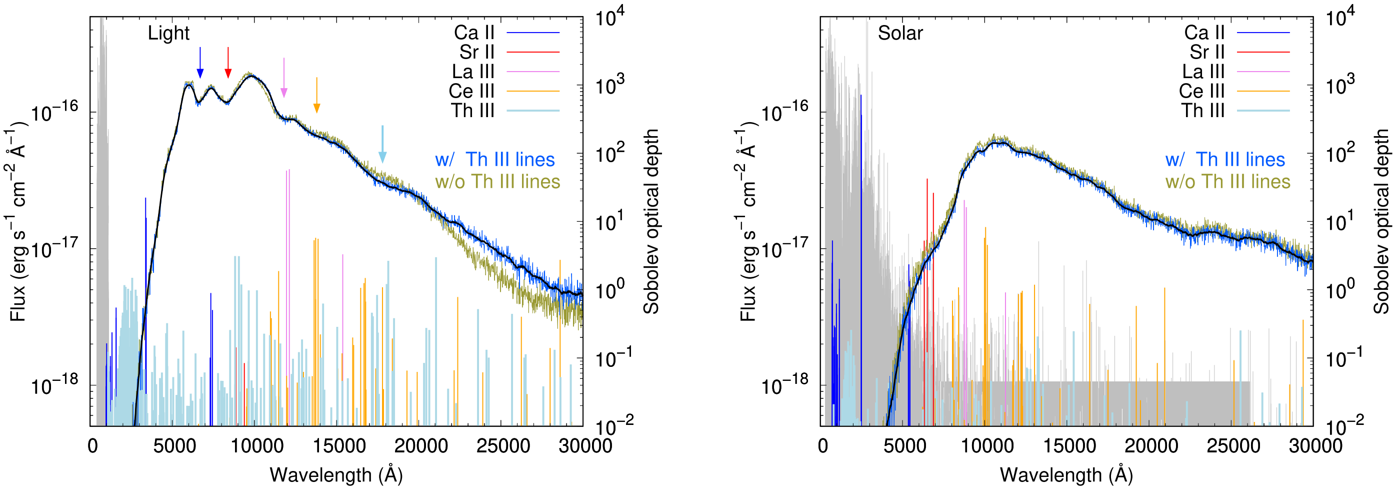

Figure 9. Left: synthetic spectrum (blue and black curves as original and smoothed results, respectively) and Sobolev optical depth of each transition (vertical lines) at $t = 1.5$ days for the L model. The flux is presented by assuming the source at 40 Mpc as that for GW170817/AT2017gfo. We plot the Sobolev optical depths of spectroscopically accurate lines in the ejecta at $v = 0.13c$. The positions of lines are blueshifted according to $v = 0.13c$. The temperature in the ejecta at $v = 0.13c$ is $T \sim 7000$ K. The synthetic spectrum without Th III lines is also shown for comparison purposes (dark yellow curve). The absorption feature produced by each element is indicated by an arrow with the same color in the legend. Note that the Ca II and Sr II features (indicated by blue and red arrows, respectively) show too large Doppler shifts to be consistent with the positions of their lines. Right: same as the left panel but for the S model. We plot the Sobolev optical depths of the lines in the ejecta at $v = 0.37c$, whose wavelengths are not necessarily accurate. The positions of the lines are blueshifted according to $v = 0.37c$. The temperature in the ejecta at $v = 0.37c$ is $T \sim 3700$ K.

On the other hand, for the S model (right panel), we find that the Th III lines decrease overall fluxes by $\sim$10% but do not produce any additional features. The spectrum is redder and dimmer than that in the L model. It should be noted that the wiggly features seen in the spectra are caused by the lines of heavy elements whose wavelengths are not experimentally calibrated.

These differences between the S and L models reflect the larger mass fraction of lanthanides for the former, which results in a higher total opacity. We confirmed that higher opacity in the S model shifts the photosphere outward compared to that in the L model. As a result, the photospheric temperature in the S model is lower and the Th III lines are weak (Figure 3). Thus, in our models, the larger mass fraction of Th is not necessarily an advantage in producing the Th III features (see also Section 4).

To see the time evolution of the spectra, we show the synthetic spectra for the L model at $t = 1.5$ and 2.5 days as blue lines in the left panels of Figure 10, focusing on the NIR region. The spectra without Th III lines are also shown by dark yellow lines. To see the effects of the Th III lines more clearly, the right panels of Figure 10 show ratios of the synthetic spectra to the Planck function. It should be cautioned that we do not intend to present the Planck function as the continuum but just for the purposes of comparison for each spectrum. We plot only the smoothed spectra for visualization.

It can be seen that the Th III feature at $\lambda \sim 18000$ Å becomes weaker (i.e., the difference between the blue and dark yellow lines becomes smaller) as time progresses. Although it may still be recognizable at $t = 2.5$ days, the feature completely disappears at $t = 3.5$ days (not shown in the figure). This is because of the temperature dependence of the Th III lines as described in Section 2.3. In our calculations, the temperature of the ejecta at $v > 0.1c$ drops below $\sim$4000 K at $\sim$3 days, at which time Th III disappears (Figures 7 and 8). This suggests that, to detect the Th III features in the photospheric spectra, we need early-time observations during the epochs when the ejecta temperature is high enough (see Section 4 for more discussion).

3.2. Conditions for Producing Thorium Features

To explore the conditions in which the Th absorption feature is observable, we vary the mass fractions of lanthanides ($Z = 57$–71) and those of elements with $Z \geqslant 82$, hereafter denoted as X (lan) and X ($Z \geqslant 82$), respectively, from the original values in the L model. Although we can in principle assume extreme cases with, for example, a much larger amount of actinides, we avoid such cases; we impose the mass fractions so that the ratio of actinides to lanthanides is kept by a factor of up to 3 to the fiducial ratio. This is because some metal-poor stars in the Galactic halo, known as "actinide-boost" stars, exhibit enhanced Th abundances whose ratio to lanthanides are by a factor of up to 3 with respect to the solar ratio (C. Siqueira Mello et al. 2013; E. M. Holmbeck et al. 2018; V. M. Placco et al. 2023). Note that, as can be seen in the left panel of Figure 2, the ratio of Th with respect to lanthanides (at 1 yr) for the L model (the same as that for the S model) is about a factor of 2 higher than that for the solar r-residuals. This indicates that the present ratio for the L model with a half-life of ^{232}Th (14.05 Gyr) is similar to the solar value, assuming a merger event about, e.g., 13 Gyr ago (comparable to the ages of actinide-boost stars). Thus, the enhancement of X ($Z \geqslant 82$) up to a factor of 3 is consistent with the range observed in actinide-boost stars.

For all the cases with varying mass fractions, the heating rate from radioactive decay as a function of time is taken from the L model. As our abundance model is dominated by relatively light r-process elements, the heating rate is also dominated by the light nuclei. Thus, the changes in mass fractions for such heavy elements do not affect the heating rate during the relevant period of time (a few days after the merger).

We note that varying X ($Z \geqslant 82$) works effectively the same as varying only the mass fraction of Th as our line list does not include atomic data for the elements with $Z = 89$–100 except for Ac III and Th III (Section 2.1). The elements with $Z = 82$–88 do not strongly contribute to the total opacity either, as expected from their atomic properties (M. Tanaka et al. 2020;

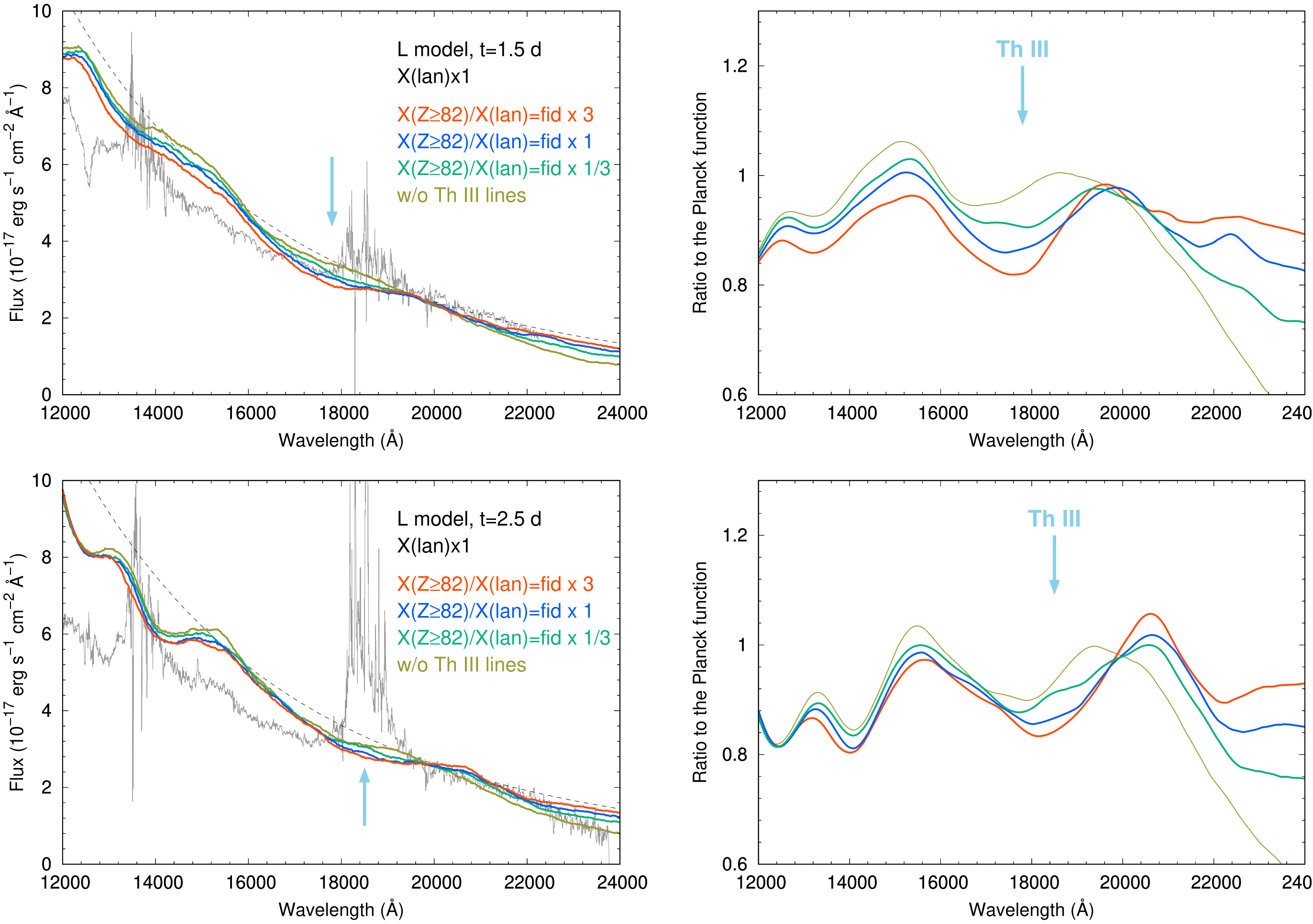

Figure 10. Left: synthetic spectra (smoothed) with the fiducial X (lan) and various X ($Z \geqslant 82$) at $t = 1.5$ (top) and 2.5 (bottom) days. The dark orange, blue, and green curves show the spectra for the ratio of actinides to lanthanides being 3, 1, and $1/3$ of the fiducial ratio, respectively, and the dark yellow curve shows the spectrum without Th III lines. The gray curve shows the observed spectrum of AT2017gfo at $t = 1.5$ and 2.5 days after merger for comparison purposes (E. Pian et al. 2017; S. J. Smartt et al. 2017). The dashed black line shows the Planck function ($T = 5300$ K, arbitrarily normalized). Right: ratios of the synthetic spectra (smoothed) to the Planck function shown in the left panel.

N. Domoto et al. 2022). C. J. Fontes et al. (2023) suggest that other actinides ($Z > 90$), especially Pa ($Z = 91$), may impact the opacity at NIR wavelengths. But this depends on the ejecta conditions (e.g., density, temperature, and epoch) as well as abundances. Thus, in the present simulation, those heaviest elements except for Th just work as little-opacity sources in the ejecta and are expected to not seriously affect the Th III features. Nevertheless, the effects of actinides should be investigated in the future.

The top-left panel of Figure 10 and the left panels of Figure 11 show the synthetic spectra at $t = 1.5$ days for the cases with variations of X (lan) and X ($Z \geqslant 82$). We compare the spectra for a fixed X (lan) along with variations of X ($Z \geqslant 82$) in each panel. The dark orange, blue, and green curves show the cases for the ratio of actinides to lanthanides being 3, 1, and $1/3$ of the fiducial ratio, respectively. The dark yellow curve shows the case without Th III lines. The top-right panel of Figure 10 and the right panels of Figure 11 show ratios of the synthetic spectra at $t = 1.5$ days to the Planck function in each panel.

For the cases in which X (lan) are equal to or less than the fiducial value (Figure 10 and top panels of Figure 11), we find the absorption features caused by Th III at $\lambda \sim 18000$ Å (see light blue arrows). The absorption features become stronger as the mass fraction of Th increases. In fact, the features caused by Th III are clearer for smaller X (lan) and larger ratios of actinides to lanthanides. This is because there are relatively strong lines of Ce III around $\lambda \sim 20000$ Å at rest wavelengths (see Figure 3). For the fiducial case, the Sobolev optical depths of some of the Ce III lines around $\lambda \sim 20000$ Å are larger than 1, which is comparable to those of the Th III lines at similar wavelengths. Thus, when X (lan) is smaller, the absorption features by Th III become more pronounced as the Ce III lines become weaker than the Th III lines. Although we only varied the abundances here, we confirmed that reducing the mass (and therefore the photospheric velocity) does not largely affect the Th III feature.

It is also seen that the flux at $\lambda \gtrsim 20000$ Å is enhanced when Th III lines are included. We note that this is likely affected by an assumption in the simulations. For an absorbed photon packet in the radiative transfer simulation, the comoving wavelength is assigned by sampling the emissivity by Kirchhoff's law, $j_\lambda = \alpha_\lambda B_\lambda(T)$, where j_λ, α_λ, and $B_\lambda(T)$ are the emissivity, the absorption coefficient, and the Planck function, respectively. This assumption approximately expresses line fluorescence when there is a sufficient number of lines (e.g., D. Kasen et al. 2006). However, for the present cases, the emissivity in the NIR wavelengths tends to depend on the

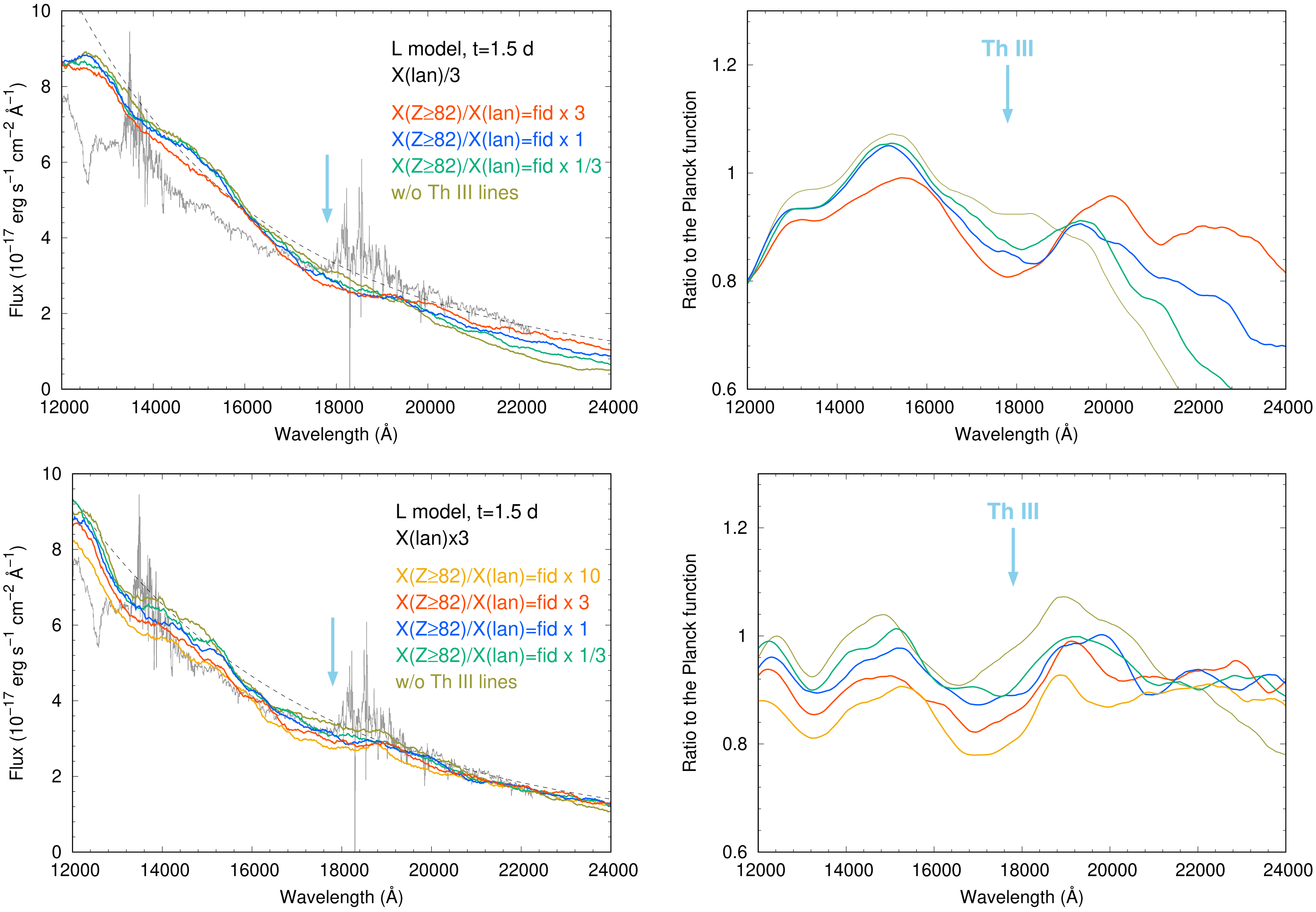

Figure 11. Same as top panels of Figure 10, but with the X (lan) reduced (top) or increased (bottom) by a factor of 3 from the original value in the L model. The temperature of the Planck function is $T = 6000$ and 4500 K for the top and bottom panels, respectively.

relatively small number of strong transitions, mainly by Ce III and Th III. Thus, the amount of Th directly affects the emissivity and resulting fluxes at $\lambda \gtrsim 20000$ Å, and its effect is larger for smaller X (lan).

For the cases in which X (lan) is larger than the fiducial value (bottom panels of Figure 11), while the increased mass fractions of actinides make the overall fluxes smaller, the effects of Th III lines on absorption features are not clear. For example, when the ratio of actinides to lanthanides is 10 times larger than the fiducial ratio (orange curves in bottom panels of Figure 11), we find the center of the decreased flux ratio being only slightly shifted toward $\lambda \sim 18000$ Å. In fact, even if X (lan) is increased further, the flux decreases overall regardless of wavelength, and no clear absorption can be seen. This is because a larger X (lan) results in a higher total opacity, as described in the case of the S model. This makes the photospheric temperature lower and the absorption features of Th III be suppressed.

4. Discussion

Our results suggest that the Th III features appear in the kilonova photospheric spectra if X (lan) is smaller than $\sim 6 \times 10^{-4}$ (the fiducial value in the L model) and the ratio of actinides to lanthanides is similar to or larger than the solar r-process value in the line-forming region. As shown in Figure 12, the L model mainly consists of high-$Y_{\rm e}$ (>0.3) components that are responsible for relatively light r-process elements, and a small fraction of low-$Y_{\rm e}$ components that are responsible for heavier elements. This demonstrates that we may be able to detect the Th III features in the spectra if the bulk of the high-$Y_{\rm e}$ ejecta has such a mixture of low-$Y_{\rm e}$ components above the photosphere.

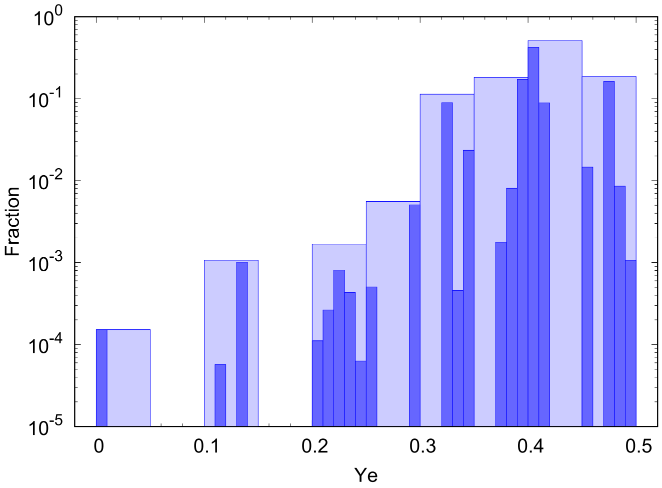

Figure 12. Histogram of electron fraction $Y_{\rm e}$ for the L model. Denser colors show the histograms with an original interval ($\Delta Y_{\rm e} = 0.01$), while lighter colors show those with a grouped interval ($\Delta Y_{\rm e} = 0.05$).

Excess of the actinide-to-lanthanide ratio, up to about a factor of 3 with respect to the solar *r*-process value, has been observed in actinide-boost stars, a subclass (about a third) of *r*-process-enhanced stars in the Galactic halo (C. Siqueira Mello et al. 2013; E. M. Holmbeck et al. 2018; V. M. Placco et al. 2023). Recent nucleosynthesis studies suggest that the mergers of black hole–NS binaries (S. Wanajo et al. 2022) or unequal-mass NSs (S. Fujibayashi et al. 2023) result in high actinide-to-lanthanide ratios because of the very low Y_e (∼0.04–0.06) in the dynamical ejecta. The kilonovae associated with the GWs from such merger events may be promising candidates for Th detection in the future.

The main uncertainty in the present results arises from the *gf*-values of the Th III lines. As the experimental *gf*-values for the NIR lines are not available, we estimated them by using the relative intensities measured by experiments (R.J. Engleman 2003). However, the estimate depends on the temperature adopted using the measured intensities (Equation (1)). In addition, there is a scatter between the measured and calculated values by roughly a factor of 3 (Figure 1), as mentioned in Section 2.1. The required mass fraction of Th to detect the Th III features roughly scales by the *gf*-values; if the *gf*-values were larger by a factor of 3, the required mass fraction of Th would become smaller by a factor of 3, and vice versa. To determine the exact *gf*-values for the Th III lines, more experimental measurements are necessary in the NIR region.

Furthermore, the *gf*-values of the Ce III lines are also a source of uncertainty in the Th features. As discussed in Section 3.2, the strength of the Th features ($\lambda \sim 18000$ Å) is affected by the Ce III lines around 20000 Å at rest wavelength. For the Ce III lines in our line list (N. Domoto et al. 2022), although the wavelengths and energy levels are experimentally accurate, the *gf*-values are adopted from a theoretical calculation (M. Tanaka et al. 2020) due to the lack of experiments, except for the strongest lines at $\lambda \sim 16000$ Å (N. Domoto et al. 2023; G. Gaigalas et al. 2024). Thus, more experimental measurements for the Ce III lines are also necessary to determine the exact *gf*-values.

It should be noted that the conditions to detect the Th III features suggested here is not necessarily the unique and only solution. Our models prefer an abundance model dominated by relatively light *r*-process elements for the Th III features to appear in the spectra. This is because the photospheric temperature lies in an appropriate range for the presence of Th III in the L model, but goes outside of this range in the S model. However, the photospheric temperature in this study depends on the opacity under the assumption of our simplistic homogeneous distribution of the elements. If the condition of a photospheric temperature $T = 5000$–7000 K with a larger mass fractions of Th (and lanthanides) were realized in more realistic ejecta profiles, the Th III features would become even stronger than those presented here (see, e.g., K. Kawaguchi et al. 2023, 2024, for the density and Y_e structure of the ejecta from self-consistent merger simulations). This possibility cannot be tested in our framework, because the opacity and temperature are coupled based on the assumed abundance distribution in the simulations.

Another caveat is that our calculations assume LTE. According to the temperature dependence of the Th III lines under LTE, we require early-time observations to detect the Th III features. However, the assumption of LTE may not be valid in the low-density regions of ejecta. Non-LTE effects may modify the ionization fraction and temperature structure in the ejecta with time, i.e., with decreasing density, which leads to overionization (K. Hotokezaka et al. 2021; Q. Pognan et al. 2022b). For example, it has been shown that T_e can stay around a few 1000 K, which keeps about a few tens of percent of heavy elements in doubly ionized states even at 20 days (K. Hotokezaka et al. 2021; Q. Pognan et al. 2023). This may allow us to continue finding the Th III features for a longer duration than that presented here, e.g., even after ∼3 days after merger.

In this paper, we do not attempt to identify Th III in the spectra of AT2017gfo. Although we showed the spectrum of AT2017gfo for comparison purposes in the left panels of Figures 10 and 11, it is difficult to judge the existence of the feature around $\lambda \sim 18000$ Å due to the strong telluric absorption. To observationally confirm the absorption features by Th III in the future, observations from space or high-altitude sites with no or little of Earth's atmosphere are necessary. For a GW170817-like kilonova associated with a detection of a GW at $\lesssim$200 Mpc (a design detection limit of GWs from NS mergers for LIGO/Virgo), observations with JWST/NIRSpec (P. Jakobsen et al. 2022; T. Böker et al. 2023) or upcoming telescopes at high altitude such as Tokyo Atacama Observatory (TAO; Y. Yoshii et al. 2010) will give sufficient signal-to-noise ratio to find the Th III features in the photospheric spectra.

5. Conclusions

We have explored signatures of the elements beyond the third *r*-process peak in the photospheric spectra of kilonovae. We constructed a line list of Ra II, Ac III, and Th III with an anticipation that their atomic properties are analogous to those of Ca II/Sr II, La III, and Ce III, respectively, which tend to produce strong absorption features in kilonova spectra. By systematically calculating the strength of bound–bound transitions using this line list, we have found that Th III is the most promising species that shows comparably strong lines in the NIR wavelengths to, e.g., Ce III lines. This is because Th III has dense low-lying energy levels and lines with relatively large *gf*-values, which make the Sobolev optical depths of the lines relatively large. Although the Ra II and Ac III lines might stand out from other lines in the optical wavelengths in cases where the light *r*-process elements are absent, we need experimentally calibrated atomic data for more lanthanides to fully verify this possibility.

We performed radiative transfer simulations to obtain synthetic spectra of kilonovae. We have shown that the Th III lines produce broad absorption features at $\lambda \sim 18000$ Å in the spectra from ∼1 days after merger if $X(\mathrm{lan}) \lesssim 6 \times 10^{-4}$ and the ratio of actinides to lanthanides is larger than the solar *r*-process value in the line-forming region. This suggests that we may be able to detect such signatures of Th if the bulk of high-Y_e ejecta has a mixture of a small fraction of low-Y_e components above the photosphere. Such conditions may be realized in the mergers of black hole–NS binaries or unequal-mass NSs. If we are able to detect the signatures caused by Th, in turn it will provide unambiguous evidence that the third *r*-process peak and heavier elements are synthesized in the ejecta of NS mergers. To detect the Th absorption features, observations from space or high-altitude sites are important, as the wavelength region of the Th features overlaps with that affected by strong telluric absorption.

Acknowledgments

We thank C.J. Fontes for helping us to collect the references on the experimental data of Th lines. Numerical simulations presented in this paper were carried out on Cray XC50 at the Center for Computational Astrophysics, National Astronomical Observatory of Japan. N.D. acknowledges support from the Graduate Program on Physics for the Universe (GP-PU) at Tohoku University. This work was supported by the JST FOREST Program (grant Nos. JPMJFR212Y and JPMJFR2136), the NIFS Collaborative Research Program (grant No. NIFS22KIIF005), the Grant-in-Aid for JSPS Fellows (grant No. 22KJ0317), and Grants-in-Aid for Scientific Research from JSPS (grant Nos. 20H00158, 21H04997, 23H00127, 23H04891, 23H04894, and 23H05432).

Appendix
Updated Transition Probabilities of Th III Lines

We summarize the *gf*-values of Th III lines estimated by using the measured line intensities in Table 2. The listed lines are overlapped with those in Table 5 of N. Domoto et al. (2022) but with the updated *gf*-values (see Section 2.1).

Table 2
Summary of Lines for Th III Whose *gf*-values Are Estimated from the Measured Line Intensities

	λ_{vac}[a] (Å)	λ_{air}[b] (Å)	Lower Level	E_{lower}[c] (cm^{-1})	Upper Level	E_{upper}[d] (cm^{-1})	log *gf*[e]
Th III	10046.6355	10043.8821	$5f6d\ ^{3}\mathrm{H}^{o}_{4}$	0.00000	$6d7s\ ^{3}\mathrm{D}_{3}$	9953.58098	−2.192
	10257.0203	10254.2099	$5f6d$	6288.2212	$6d7s\ ^{1}\mathrm{D}_{2}$	16037.64127	−1.441
	10260.9778	10258.1662	$5f6d\ ^{3}\mathrm{G}^{o}_{4}$	8141.74929	$5f^{2}\ ^{3}\mathrm{H}_{5}$	17887.40925	0.606
	10532.8696	10529.9844	$5f6d\ ^{3}\mathrm{G}^{o}_{5}$	11276.80704	$5f^{2}\ ^{3}\mathrm{H}_{6}$	20770.89593	0.877
	10581.3571	10578.4587	$5f6d\ ^{3}\mathrm{H}^{o}_{6}$	8436.8256	$5f^{2}\ ^{3}\mathrm{H}_{5}$	17887.40925	−1.367
	10706.5771	10703.6448	$5f6d\ ^{1}\mathrm{H}^{o}_{5}$	19009.90952	$5f^{2}\ ^{3}\mathrm{I}_{6}$	28349.96275	1.153
	11216.3023	11213.2317	$6d^{2}\ ^{3}\mathrm{F}_{4}$	6537.81726	$5f6d\ ^{1}\mathrm{F}^{o}_{3}$	15453.41152	−1.118
	11227.3116	11224.2381	$5f6d$	8980.55749	$5f^{2}\ ^{3}\mathrm{H}_{5}$	17887.40925	0.140
	11428.8103	11425.6821	$7s^{2}\ ^{1}\mathrm{S}_{0}$	11961.1316	$5f6d\ ^{1}\mathrm{P}^{o}_{1}$	20710.9487	−0.916
	11516.6200	11513.4679	$5f6d\ ^{3}\mathrm{D}^{o}_{2}$	10180.76952	$5f^{2}\ ^{3}\mathrm{F}_{2}$	18863.86913	−1.192
	11720.8814	11717.6740	$6d^{2}$	4676.43214	$5f6d\ ^{3}\mathrm{P}^{o}_{2}$	13208.2137	−1.912
	11810.5436	11807.3118	$6d^{2}\ ^{1}\mathrm{G}_{4}$	10542.89973	$5f6d\ ^{1}\mathrm{H}^{o}_{5}$	19009.90952	0.260
	12081.2271	12077.9218	$6d7s\ ^{3}\mathrm{D}_{2}$	7176.10661	$5f6d\ ^{1}\mathrm{F}^{o}_{3}$	15453.41152	−1.481
	12320.5004	12317.1302	$5f6d\ ^{3}\mathrm{D}^{o}_{1}$	7921.08782	$6d7s\ ^{1}\mathrm{D}_{2}$	16037.64127	−0.629
	12726.1743	12722.6939	$6d^{2}\ ^{3}\mathrm{F}_{2}$	63.26679	$5f6d\ ^{3}\mathrm{D}^{o}_{1}$	7921.08782	−1.374
	12918.7449	12915.2122	$5f6d\ ^{3}\mathrm{P}^{o}_{1}$	11123.1791	$5f^{2}\ ^{3}\mathrm{F}_{2}$	18863.86913	−1.117
	13075.4606	13071.8853	$5f7s$	7500.60523	$5f^{2}\ ^{3}\mathrm{H}_{4}$	15148.51938	−0.782
	13102.2536	13098.6710	$5f6d\ ^{3}\mathrm{P}^{o}_{2}$	13208.2137	$5f^{2}\ ^{3}\mathrm{F}_{3}$	20840.48853	−1.095
	13445.6702	13441.9944	$6d^{2}\ ^{3}\mathrm{F}_{2}$	63.26579	$5f7s$	7500.60523	−2.294
	13465.3195	13461.6384	$5f7s$	2527.09550	$6d7s\ ^{3}\mathrm{D}_{3}$	9953.58098	−1.298
	13577.6105	13573.8999	$5f6d\ ^{3}\mathrm{F}^{o}_{2}$	510.75823	$6d^{2}\ ^{3}\mathrm{P}_{1}$	7875.8244	−2.783
	13596.9359	13593.2199	$5f6d$	3188.30107	$6d^{2}\ ^{1}\mathrm{G}_{4}$	10542.89873	−2.180
	14271.9111	14268.0108	$5f6d\ ^{3}\mathrm{G}^{o}_{4}$	8141.74929	$5f^{2}\ ^{3}\mathrm{H}_{4}$	15148.51938	−1.264
	14363.1448	14359.2196	$5f6d\ ^{1}\mathrm{H}^{o}_{5}$	19009.90952	$5f^{2}\ ^{1}\mathrm{G}_{4}$	25972.17312	−0.063
	14766.5150	14762.4802	$5f7s\ ^{3}\mathrm{F}^{o}_{2}$	3181.5024	$6d7s\ ^{3}\mathrm{D}_{3}$	9953.58098	−2.494
	14781.3544	14777.3156	$5f6d$	3188.30107	$6d7s\ ^{3}\mathrm{D}_{3}$	9953.58098	−1.406
	14958.5620	14954.4751	$6d^{2}\ ^{3}\mathrm{F}_{3}$	4056.01548	$5f6d\ ^{3}\mathrm{D}^{o}_{3}$	10741.15004	−1.863
	15002.9667	14998.8677	$5f6d\ ^{3}\mathrm{F}^{o}_{2}$	510.75823	$6d7s\ ^{3}\mathrm{D}_{2}$	7176.10661	−1.468
	15127.2149	15123.0820	$5f6d\ ^{3}\mathrm{G}^{o}_{5}$	11276.80704	$5f^{2}\ ^{3}\mathrm{H}_{5}$	17887.40925	−1.056
	15295.6248	15291.4462	$5f6d\ ^{3}\mathrm{H}^{o}_{4}$	0.00000	$6d^{2}\ ^{3}\mathrm{F}_{4}$	6537.81726	−1.660
	15511.6993	15507.4619	$6d^{2}$	4676.43214	$5f6d\ ^{3}\mathrm{P}^{o}_{1}$	11123.1791	−1.650
	16064.3737	16059.9870	$6d^{2}\ ^{3}\mathrm{F}_{2}$	63.26579	$5f6d$	6288.2212	−2.912
	16212.8109	16208.3829	$5f6d$	8980.55749	$5f^{2}\ ^{3}\mathrm{H}_{4}$	15148.51938	−1.981
	16327.1959	16322.7367	$6d^{2}\ ^{3}\mathrm{F}_{3}$	4056.01548	$5f6d\ ^{3}\mathrm{D}^{o}_{2}$	10180.76592	−1.451
	16488.8131	16484.3100	$6d^{2}$	4676.43214	$5f6d\ ^{3}\mathrm{D}^{o}_{3}$	10741.15004	−0.608
	16577.9550	16573.4277	$6d7s\ ^{3}\mathrm{D}_{2}$	7176.10661	$5f6d\ ^{3}\mathrm{P}^{o}_{2}$	13208.2137	−1.647
	17073.9505	17069.2883	$5f6d\ ^{3}\mathrm{D}^{o}_{2}$	10180.76592	$6d7s\ ^{1}\mathrm{D}_{2}$	16037.64127	−1.647
	17494.5296	17489.7530	$5f6d$	4826.82620	$6d^{2}\ ^{1}\mathrm{G}_{4}$	10542.89873	−0.961
	17517.0190	17512.2362	$6d7s\ ^{3}\mathrm{D}_{1}$	5523.8809	$5f6d\ ^{3}\mathrm{P}^{o}_{0}$	11232.6148	−1.675
	17814.4804	17809.6167	$5f6d$	4826.82620	$6d^{2}\ ^{3}\mathrm{P}_{2}$	10440.2372	−2.535
	17859.3810	17854.5071	$6d7s\ ^{3}\mathrm{D}_{1}$	5523.8809	$5f6d\ ^{3}\mathrm{P}^{o}_{1}$	11123.1791	−1.699
	18182.3784	18177.4147	$6d7s\ ^{3}\mathrm{D}_{3}$	9953.58089	$5f6d\ ^{1}\mathrm{F}^{o}_{3}$	15453.41152	−2.694
	18240.3369	18235.3574	$5f6d\ ^{3}\mathrm{G}^{o}_{3}$	5060.54386	$6d^{2}\ ^{1}\mathrm{G}_{4}$	10542.89973	−1.712
	18588.4201	18583.3459	$5f6d\ ^{3}\mathrm{G}^{o}_{3}$	5060.54386	$6d^{2}\ ^{3}\mathrm{P}_{2}$	10440.2372	−2.499
	18880.4240	18875.2703	$5f6d\ ^{3}\mathrm{D}^{o}_{3}$	10741.15004	$6d7s\ ^{1}\mathrm{D}_{2}$	16037.64127	−1.647
	19947.4412	19941.9972	$6d^{2}\ ^{3}\mathrm{P}_{2}$	10440.2372	$5f6d\ ^{1}\mathrm{F}^{o}_{3}$	15453.41152	−0.500

Table 2
(Continued)

λ_{vac}[a] (Å)	λ_{air}[b] (Å)	Lower Level	E_{lower}[c] (cm^{-1})	Upper Level	E_{upper}[d] (cm^{-1})	log gf[e]
19947.6467	19942.2026	$5f6d\ ^{3}\mathrm{F}^{o}_{2}$	510.75823	$6d7s\ ^{3}\mathrm{D}_{1}$	5523.8809	−1.201
20010.8977	20005.4364	$6d^{2}\ ^{3}\mathrm{F}_{2}$	63.26679	$5f6d\ ^{3}\mathrm{G}^{o}_{3}$	5060.54386	−1.296
20306.4569	20300.9151	$6d^{2}\ ^{3}\mathrm{F}_{3}$	4056.01548	$5f6d$	8980.55749	−0.629
20364.4720	20358.9144	$6d^{2}\ ^{1}\mathrm{G}_{4}$	10542.89873	$5f6d\ ^{1}\mathrm{F}^{o}_{3}$	15453.41152	−0.596
20437.2044	20431.6271	$5f6d\ ^{3}\mathrm{G}^{o}_{3}$	5060.54386	$6d7s\ ^{3}\mathrm{D}_{3}$	9953.58098	−1.990
20992.7054	20986.9770	$6d^{2}\ ^{3}\mathrm{F}_{2}$	63.26679	$5f6d$	4826.82620	−0.844
21101.5437	21095.7856	$6d^{2}\ ^{3}\mathrm{F}_{4}$	6537.81726	$5f6d\ ^{3}\mathrm{G}^{o}_{5}$	11276.80704	0.079
21398.121	21392.283	$6d7s\ ^{1}\mathrm{D}_{2}$	16037.64127	$5f6d\ ^{1}\mathrm{P}^{o}_{1}$	20710.9487	−0.683
21473.5815	21467.7221	$6d7s\ ^{3}\mathrm{D}_{1}$	5523.8809	$5f6d\ ^{3}\mathrm{D}^{o}_{2}$	10180.76592	−3.099
21509.9507	21504.0814	$5f7s$	2527.09550	$6d7s\ ^{3}\mathrm{D}_{2}$	7176.10661	−1.132
22689.2716	22683.0813	$5f6d\ ^{3}\mathrm{D}^{o}_{3}$	10741.15004	$5f^{2}\ ^{3}\mathrm{H}_{4}$	15148.51938	−1.492
23628.9815	23622.5353	$5f7s\ ^{3}\mathrm{F}^{o}_{4}$	6310.80773	$6d^{2}\ ^{1}\mathrm{G}_{4}$	10542.89873	−1.487
23790.6455	23784.1553	$6d^{2}\ ^{3}\mathrm{F}_{4}$	6537.81726	$5f6d\ ^{3}\mathrm{D}^{o}_{3}$	10741.15004	−0.956
24005.7196	23999.1709	$5f6d\ ^{3}\mathrm{F}^{o}_{2}$	510.75823	$6d^{2}$	4676.43214	−1.534
24475.4075	24468.7309	$6d^{2}\ ^{3}\mathrm{F}_{3}$	4056.01548	$5f6d\ ^{3}\mathrm{G}^{o}_{4}$	8141.74929	−0.156
25335.2327	25328.3219	$6d7s\ ^{3}\mathrm{D}_{2}$	7176.10661	$5f6d\ ^{3}\mathrm{P}^{o}_{1}$	11123.1791	−1.816
25897.4091	25890.3452	$5f^{2}\ ^{3}\mathrm{H}_{4}$	15148.51938	$5f6d\ ^{1}\mathrm{H}^{o}_{5}$	19009.90952	−1.317
27282.451	27275.010	$5f6d$	6288.2212	$6d7s\ ^{3}\mathrm{D}_{3}$	9953.58098	−2.915
27451.6126	27444.1255	$5f7s\ ^{3}\mathrm{F}^{o}_{4}$	6310.80773	$6d7s\ ^{3}\mathrm{D}_{3}$	9953.58098	−0.763
28050.1492	28042.4991	$6d7s\ ^{3}\mathrm{D}_{2}$	7176.10661	$5f6d\ ^{3}\mathrm{D}^{o}_{3}$	10741.15004	−1.290
28206.6978	28199.0051	$5f6d\ ^{3}\mathrm{F}^{o}_{2}$	510.75823	$6d^{2}\ ^{3}\mathrm{F}_{3}$	4056.0148	−2.009
29790.362	29782.238	$6d^{2}\ ^{3}\mathrm{P}_{1}$	7875.8244	$5f6d\ ^{3}\mathrm{P}^{o}_{0}$	11232.6148	−2.705
29855.0580	29846.9163	$5f6d$	3188.30107	$6d^{2}\ ^{3}\mathrm{F}_{4}$	6537.81726	−1.151
30725.433	30717.054	$6d7s\ ^{3}\mathrm{D}_{3}$	9953.58098	$5f6d\ ^{3}\mathrm{P}^{o}_{2}$	13208.2137	−1.194
30794.295	30785.898	$6d^{2}\ ^{3}\mathrm{P}_{1}$	7875.8244	$5f6d\ ^{3}\mathrm{P}^{o}_{1}$	11123.1791	−1.409
30819.9112	30811.5068	$6d^{2}$	4676.43214	$5f6d\ ^{3}\mathrm{D}^{o}_{1}$	7921.08782	−1.623
32069.418	32060.673	$6d^{2}\ ^{3}\mathrm{F}_{2}$	63.26679	$5f7s\ ^{3}\mathrm{F}^{o}_{2}$	3181.5024	−2.526
32869.938	32860.976	$5f7s$	7500.60523	$6d^{2}\ ^{1}\mathrm{G}_{4}$	10542.89873	−1.330
33281.644	33272.569	$6d7s\ ^{3}\mathrm{D}_{2}$	7176.10661	$5f6d\ ^{3}\mathrm{D}^{o}_{2}$	10180.76592	−1.764
34017.864	34008.588	$5f7s$	7500.60523	$6d^{2}\ ^{3}\mathrm{P}_{2}$	10440.2372	−1.558
35322.815	35313.184	$6d^{2}\ ^{3}\mathrm{P}_{0}$	5090.0564	$5f6d\ ^{3}\mathrm{D}^{o}_{1}$	7921.08782	−1.411
35408.695	35398.940	$6d^{2}$	4676.43214	$5f7s$	7500.60523	−1.236
36127.474	36117.624	$6d^{2}\ ^{3}\mathrm{P}_{2}$	10440.2372	$5f6d\ ^{3}\mathrm{P}^{o}_{2}$	13208.2137	−2.332
40587.237	40576.172	$6d^{2}\ ^{3}\mathrm{F}_{2}$	63.26679	$5f7s$	2527.09550	−1.042
40766.811	40755.697	$5f7s$	7500.60523	$6d7s\ ^{3}\mathrm{D}_{3}$	9953.58098	−2.566
40937.632	40926.471	$6d^{2}\ ^{3}\mathrm{F}_{4}$	6537.81726	$5f6d$	8980.55749	−1.965
41715.214	41703.842	$6d7s\ ^{3}\mathrm{D}_{1}$	5523.8809	$5f6d\ ^{3}\mathrm{D}^{o}_{1}$	7921.08809	−2.281
42566.226	42554.621	$5f6d$	4826.82620	$6d7s\ ^{3}\mathrm{D}_{2}$	7176.10661	−2.341
42691.649	42680.010	$5f7s\ ^{3}\mathrm{F}^{o}_{2}$	3181.5024	$6d7s\ ^{3}\mathrm{D}_{1}$	5523.8809	−1.443
43385.049	43373.221	$6d^{2}\ ^{3}\mathrm{P}_{1}$	7875.8244	$5f6d\ ^{3}\mathrm{D}^{o}_{2}$	10180.76592	−1.090
44349.984	44337.894	$6d^{2}\ ^{3}\mathrm{F}_{3}$	4056.01548	$5f7s\ ^{3}\mathrm{F}^{o}_{4}$	6310.80773	−1.474
46525.983	46513.300	$5f7s$	2527.09550	$6d^{2}$	4676.43214	−1.510

Notes.

[a] Vacuum transition wavelength.

[b] Air transition wavelength.

[c] Lower energy level.

[d] Upper energy level.

[e] gf-value estimated in Section 2.1.

ORCID iDs

Nanae Domoto https://orcid.org/0000-0002-7415-7954
Shinya Wanajo https://orcid.org/0000-0002-4759-7794
Masaomi Tanaka https://orcid.org/0000-0001-8253-6850
Daiji Kato https://orcid.org/0000-0002-5302-073X
Kenta Hotokezaka https://orcid.org/0000-0002-2502-3730

References

Abbott, B. P., Abbott, R., Abbott, T. D., et al. 2017a, PhRvL, 119, 161101
Abbott, B. P., Abbott, R., Abbott, T. D., et al. 2017b, ApJL, 848, L12
Arcavi, I., Hosseinzadeh, G., Howell, D. A., et al. 2017, Natur, 551, 64
Barnes, J., Kasen, D., Wu, M.-R., & Martínez-Pinedo, G. 2016, ApJ, 829, 110
Biémont, E., Palmeri, P., Quinet, P., Zhang, Z. G., & Svanberg, S. 2002, ApJ, 567, 1276

Böker, T., Beck, T. L., Birkmann, S. M., et al. 2023, PASP, 135, 038001
Coulter, D. A., Foley, R. J., Kilpatrick, C. D., et al. 2017, Sci, 358, 1556
Cowan, J. J., Sneden, C., Beers, T. C., et al. 2005, ApJ, 627, 238
Domoto, N., Lee, J.-J., Tanaka, M., et al. 2023, ApJ, 956, 113
Domoto, N., Tanaka, M., Kato, D., et al. 2022, ApJ, 939, 8
Domoto, N., Tanaka, M., Wanajo, S., & Kawaguchi, K. 2021, ApJ, 913, 26
Eichler, D., Livio, M., Piran, T., & Schramm, D. N. 1989, Natur, 340, 126
Engleman, R. J. 2003, JQSRT, 78, 1
Evans, P. A., Cenko, S. B., Kennea, J. A., et al. 2017, Sci, 358, 1565
Flörs, A., Silva, R. F., Deprince, J., et al. 2023, MNRAS, 524, 3083
Fontes, C. J., Fryer, C. L., Wollaeger, R. T., Mumpower, M. R., & Sprouse, T. M. 2023, MNRAS, 519, 2862
Freiburghaus, C., Rosswog, S., & Thielemann, F. K. 1999, ApJL, 525, L121
Fujibayashi, S., Kiuchi, K., Wanajo, S., et al. 2023, ApJ, 942, 39
Gaigalas, G., Rynkun, P., Domoto, N., et al. 2024, MNRAS, 530, 5220
Gillanders, J. H., McCann, M., Sim, S. A., Smartt, S. J., & Ballance, C. P. 2021, MNRAS, 506, 3560
Gillanders, J. H., Smartt, S. J., Sim, S. A., Bauswein, A., & Goriely, S. 2022, MNRAS, 515, 631
Goriely, S., Bauswein, A., & Janka, H.-T. 2011, ApJL, 738, L32
Holmbeck, E. M., Beers, T. C., Roederer, I. U., et al. 2018, ApJL, 859, L24
Honda, S., Aoki, W., Ishimaru, Y., Wanajo, S., & Ryan, S. G. 2006, ApJ, 643, 1180
Hotokezaka, K., Tanaka, M., Kato, D., & Gaigalas, G. 2021, MNRAS, 506, 5863
Hotokezaka, K., Tanaka, M., Kato, D., & Gaigalas, G. 2022, MNRAS, 515, L89
Hotokezaka, K., Tanaka, M., Kato, D., & Gaigalas, G. 2023, MNRAS, 526, L155
Jakobsen, P., Ferruit, P., Alves de Oliveira, C., et al. 2022, A&A, 661, A80
Kasen, D., Badnell, N. R., & Barnes, J. 2013, ApJ, 774, 25
Kasen, D., Metzger, B., Barnes, J., Quataert, E., & Ramirez-Ruiz, E. 2017, Natur, 551, 80
Kasen, D., Thomas, R. C., & Nugent, P. 2006, ApJ, 651, 366
Kasliwal, M. M., Kasen, D., Lau, R. M., et al. 2022, MNRAS, 510, L7
Kawaguchi, K., Domoto, N., Fujibayashi, S., et al. 2024, MNRAS, 535, 3711
Kawaguchi, K., Fujibayashi, S., Domoto, N., et al. 2023, MNRAS, 525, 3384
Kawaguchi, K., Shibata, M., & Tanaka, M. 2018, ApJL, 865, L21
Kawaguchi, K., Shibata, M., & Tanaka, M. 2020, ApJ, 889, 171
Korobkin, O., Rosswog, S., Arcones, A., & Winteler, C. 2012, MNRAS, 426, 1940
Kramida, A. 2022, Atoms, 10, 42
Kramida, A., Ralchenko, Y., Reader, J. & NIST ASD Team 2024, Atomic Spectra Database (ver. 5.12), NIST, doi:10.18434/T4W30F
Kullmann, I., Goriely, S., Just, O., Bauswein, A., & Janka, H.-T. 2023, MNRAS, 523, 2551
Kupka, F., Piskunov, N., Ryabchikova, T. A., Stempels, H. C., & Weiss, W. W. 1999, A&AS, 138, 119
Lattimer, J. M., & Schramm, D. N. 1974, ApJL, 192, L145
Li, L.-X., & Paczyński, B. 1998, ApJL, 507, L59
Lucy, L. B. 2003, A&A, 403, 261
Meggers, W. F., Fred, M., & Tomkins, F. S. 1957, JRNBS, 58, 297
Metzger, B. D., Martínez-Pinedo, G., Darbha, S., et al. 2010, MNRAS, 406, 2650
Palmer, B. A., & Engleman, R. 1983, Atlas of the Thorium Spectrum (Los Alamos, NM: Los Alamos National Laboratory)
Perego, A., Radice, D., & Bernuzzi, S. 2017, ApJL, 850, L37
Perego, A., Vescovi, D., Fiore, A., et al. 2022, ApJ, 925, 22
Pian, E., D'Avanzo, P., Benetti, S., et al. 2017, Natur, 551, 67
Piskunov, N. E., Kupka, F., Ryabchikova, T. A., Weiss, W. W., & Jeffery, C. S. 1995, A&AS, 112, 525
Placco, V. M., Almeida-Fernandes, F., Holmbeck, E. M., et al. 2023, ApJ, 959, 60
Pognan, Q., Grumer, J., Jerkstrand, A., & Wanajo, S. 2023, MNRAS, 526, 5220
Pognan, Q., Jerkstrand, A., & Grumer, J. 2022a, MNRAS, 513, 5174
Pognan, Q., Jerkstrand, A., & Grumer, J. 2022b, MNRAS, 510, 3806
Prantzos, N., Abia, C., Cristallo, S., Limongi, M., & Chieffi, A. 2020, MNRAS, 491, 1832
Roberts, B. M., Dzuba, V. A., & Flambaum, V. V. 2013, PhRvA, 88, 012510
Roberts, L. F., Kasen, D., Lee, W. H., & Ramirez-Ruiz, E. 2011, ApJL, 736, L21
Roederer, I. U., Lawler, J. E., Sobeck, J. S., et al. 2012, ApJS, 203, 27
Rosswog, S., Sollerman, J., Feindt, U., et al. 2018, A&A, 615, A132
Ryabchikova, T., Piskunov, N., Kurucz, R. L., et al. 2015, PhyS, 90, 054005
Safronova, U. I., Johnson, W. R., & Safronova, M. S. 2007, PhRvA, 76, 042504
Sahoo, B. K., Wansbeek, L. W., Jungmann, K., & Timmermans, R. G. E. 2009, PhRvA, 79, 052512
Shibata, M., Fujibayashi, S., Hotokezaka, K., et al. 2017, PhRvD, 96, 123012
Silva, R. F., Sampaio, J. M., Amaro, P., et al. 2022, Atoms, 10, 18
Siqueira Mello, C., Spite, M., Barbuy, B., et al. 2013, A&A, 550, A122
Smartt, S. J., Chen, T. W., Jerkstrand, A., et al. 2017, Natur, 551, 75
Sneppen, A., Damgaard, R., Watson, D., et al. 2024, A&A, 692, A134,
Sneppen, A., & Watson, D. 2023, A&A, 675, A194
Sobolev, V. V. 1960, Moving Envelopes of Stars (Cambridge, MA: Harvard Univ. Press)
Tanaka, M., Domoto, N., Aoki, W., et al. 2023, ApJ, 953, 17
Tanaka, M., & Hotokezaka, K. 2013, ApJ, 775, 113
Tanaka, M., Hotokezaka, K., Kyutoku, K., et al. 2014, ApJ, 780, 31
Tanaka, M., Kato, D., Gaigalas, G., & Kawaguchi, K. 2020, MNRAS, 496, 1369
Tanaka, M., Utsumi, Y., Mazzali, P. A., et al. 2017, PASJ, 69, 102
Tarumi, Y., Hotokezaka, K., Domoto, N., & Tanaka, M. 2023, arXiv:2302.13061
Utsumi, Y., Tanaka, M., Tominaga, N., et al. 2017, PASJ, 69, 101
Valenti, S., Sand, D. J., Yang, S., et al. 2017, ApJL, 848, L24
Villar, V. A., Cowperthwaite, P. S., Berger, E., et al. 2018, ApJL, 862, L11
Wanajo, S. 2018, ApJ, 868, 65
Wanajo, S., Fujibayashi, S., Hayashi, K., et al. 2022, arXiv:2212.04507
Wanajo, S., Sekiguchi, Y., Nishimura, N., et al. 2014, ApJL, 789, L39
Watson, D., Hansen, C. J., Selsing, J., et al. 2019, Natur, 574, 497
Wu, M.-R., Barnes, J., Martínez-Pinedo, G., & Metzger, B. D. 2019, PhRvL, 122, 062701
Yoshii, Y., Aoki, T., Doi, M., et al. 2010, Proc. SPIE, 7733, 773308
Zhu, Y., Wollaeger, R. T., Vassh, N., et al. 2018, ApJL, 863, L23